Chemosphere 280 (2021) 130659

Contents lists available at ScienceDirect

Chemosphere

journal homepage: www.elsevier.com/locate/chemosphere

Bisphenol A cleanup over MIL-100(Fe)/CoS composites: Pivotal role of Fe—S bond in regenerating Fe^{2+} ions for boosted degradation performance

Lin Wu, Chong-Chen Wang*, Hong-Yu Chu, Xiao-Hong Yi, Peng Wang, Chen Zhao, Huifen Fu**

Beijing Key Laboratory of Functional Materials for Building Structure and Environment Remediation, School of Environment and Energy Engineering, Beijing University of Civil Engineering and Architecture, Beijing, 100044, China

HIGHLIGHTS

- The MIL-100(Fe)/CoS (M*x*C*y*) composites were prepared by ball-milling.
- M50C50 exhibited superior Fenton-like catalytic activity toward BPA.
- The formed Fe—S in M50C50 boosts its activity by improving Fe^{2+} regeneration.
- M50C50 displayed good reusability and stability.

GRAPHICAL ABSTRACT

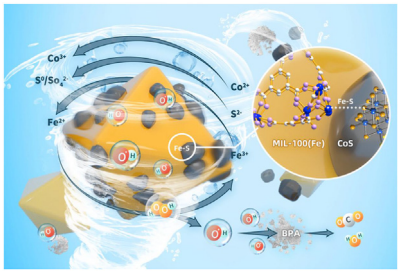

ARTICLE INFO

Article history:
Received 10 March 2021
Received in revised form
16 April 2021
Accepted 22 April 2021
Available online 27 April 2021

Handling Editor: Junfeng Niu

Keywords:
MIL-100(Fe)
CoS
Fenton oxidation
Fe—S bond
Metal-organic framework
Interfacial electron migration

ABSTRACT

Series of MIL-100(Fe)/CoS composites (M*x*C*y*) were facilely fabricated using ball-milling method. The optimum M50C50 exhibited extremely higher Fenton-like catalytic degradation activity toward bisphenol A (BPA) than the pristine MIL-100(Fe) and CoS. The significant improvement of BPA degradation was attributed to the synergetic effect between MIL-100(Fe) and CoS with the synergistic factor being 95.7%, in which the Fe—S bonds formed at the interface of the two components facilitate the Fe^{3+}/Fe^{2+} cycle by improving the electron mobility both from Co to Fe and from S to Fe. Furthermore, the influence factors like co-existing inorganic ions and pH values on the catalysis activity of M50C50 were explored. The possible reaction mechanism was proposed and confirmed by both active species capture tests and electron spin resonance (ESR) determinations. It was found that M50C50 demonstrated good reusability and water stability, in which the morphology and structure were not changed obviously after five runs' operation. To our best knowledge, it is the first work concerning the interfacial interaction of Fe-MOF/MS*x* to promote Fe^{3+}/Fe^{2+} cycle in Fe-MOFs for the purpose of organic pollutants degradation in the Fenton-like AOPs system.

© 2021 Elsevier Ltd. All rights reserved.

1. Introduction

The persistent and bio-accumulative emerging organic contaminants (EOCs) might exert potential threat to living organisms and environment due to their high toxicity (Guo et al., 2017; Xiao-

* Corresponding author.
** Corresponding author.
E-mail addresses: wangchongchen@bucea.edu.cn, chongchenwang@126.com (C.-C. Wang), fuhuifen@bucea.edu.cn (H. Fu).

https://doi.org/10.1016/j.chemosphere.2021.130659
0045-6535/© 2021 Elsevier Ltd. All rights reserved.

Hong and Chong-Chen, 2020). Just recently, different strategies like adsorption (Xu et al., 2018; Hao et al., 2019), biodegradation (Vasiliadou et al., 2013) and advanced oxidation processes (AOPs) (Shayegan et al., 2018; Peng et al., 2021) have been adopted to remove the EOCs in water. Among these methods, AOPs exhibit some merits like strong oxidizability, high degradation rate and no hazardous byproducts (Zhang et al., 2016; Ike et al., 2019). The catalyst-enhanced AOPs like Fenton and Fenton-like reactions can produce hydroxyl radicals (•OH, $E^0 = 1.9–2.7$ V) to degrade various organic pollutants (Zhang et al., 2014b; Wang and Zhuan, 2020; Zhou et al., 2020). The Fenton and Fenton-like oxidation methods are widely used in water treatment mainly for the following reasons: (i) The oxidation reaction can be carried out at room temperature and pressure, which averts the necessity of sophisticated reactor equipment; (ii) Because the quick reaction between Fe^{2+} and H_2O_2, a large amount of •OH radicals are produced in the short reaction time (Pouran et al., 2014); and (iii) The efficient mineralization enables the conversion of organic pollutants to innocuous CO_2 and H_2O (Nidheesh et al., 2013). Therefore, the Fenton and Fenton-like oxidation processes have been widely utilized to treat various wastewater like oilfield sewage (Mosteo et al., 2007), pharmaceutical wastewater (Mosteo et al., 2007), organic sludge (Mosteo et al., 2007; Umar et al., 2010) and landfill leachate (Watts and Teel, 2005; Umar et al., 2010; Yap et al., 2011).

Metal-organic frameworks (MOFs) are porous organic functional materials formed by the coordination and self-assembly of multidentate organic ligands containing O or N atom and transition metal ions (Xu et al., 2018), in which various iron-based MOFs are widely adopted as catalysts to activate H_2O_2 for accomplishing Fenton-like AOPs. The abundant nano-scale cavities and exoteric channels in frameworks can afford favorable channels for the entry of the targets to be treated as well as the discharge of the product after treatment, which helps to promote the mass transfer process of catalytic reaction (Wang et al., 2019). Besides the above-stated remarkable properties, the uniformly dispersed metal constituents in MOFs also provide sufficient active locations for catalytic reaction (Gao et al., 2017). However, like other heterogeneous Fe-based catalysts, the Fe-MOFs suffered from the limited Fe^{3+}/Fe^{2+} cycle (Zou et al., 2013), which should be further boosted in the Fenton-like AOPs for the purpose of increasing the oxidation activity. For example, Hu et al. constructed MoS_2/α-Fe_2O_3 heterojunction to achieve enhanced catalytic in the Fenton-like reaction, in which the Fe–S bond at the interface can boost the Fe^{3+}/Fe^{2+} cycle by enhancing the electron transfer from Mo to Fe (Hu et al., 2020). Inspired by this work, it was predicted that some sorts of Fe-MOFs and metal sulfides (MS*x*) can be selected to construct Fe-MOF/MS*x* to promote Fe^{3+}/Fe^{2+} cycle.

Within this paper, MIL-100(Fe) as a typical Fe-MOF and CoS were selected to construct MIL-100(Fe)/CoS (M*x*C*y*) composites with the aid of ball-milling method, in which the optimal M50C50 displayed superior bisphenol A (BPA) decomposition performance via Fenton-like AOPs. The enhancement of Fenton-like catalysis activity is contributed to the formation of Fe–S bond via the interfacial interaction between CoS and MIL-100(Fe). This work could provide an alternative approach to boost the Fe-MOFs-based heterogeneous Fenton-like catalytic reactivity.

2. Experimental

2.1. Materials and characterization

All information of the used materials and detailed characterization instruments were listed in the Electronic supplementary information (ESI).

2.2. Synthesis of MIL-100(Fe)/CoS composites

The solvothermal synthesis of octahedral MIL-100(Fe) was carried out following the method previously reported (Chen et al., 2020). Briefly, 0.11 g iron powder (Fe^0), 0.15 mL concentrated nitric acid (HNO_3) and 10.0 mL H_2O were mixed and dissolved by ultrasound for 15 min, in which 0.28 g 1,3,5-benzenetricarboxylic acid (H_3BTC) and 0.18 mL hydrofluoric acid (HF) were added. The mixture was moved into Teflon-lined stainless steel Parr bomb, and heated at 150 °C for 24 h. The harvested orange-yellow precipitates were centrifuged, washed successively with ethanol and deionized water (DI water) for 3 times, and finally dried at 60 °C under vacuum for 10 h.

Typically, 0.1 g $Co(NO_3)_2 \cdot 6H_2O$ and 0.4 g thioacetamide (TAA) were respectively dissolved in 20.0 mL ethanol, which were mixed in Teflon-lined stainless steel Parr bomb, and heated at 120 °C for 8 h. Finally, the black spherical CoS particles were collected by centrifuging, which were washed with DI water and dried at 60 °C in a vacuum oven overnight.

As shown in Scheme 1, the MIL-100(Fe)/CoS composites were synthesized with the as-obtained MIL-100(Fe) and CoS as precursors with the aid of ball milling treatment (30 Hz and 20 min). The obtained MIL-100(Fe)/CoS composites with different mass ratios can be referred as M*x*C*y*. The letters “M” and “C” are abbreviated from MIL-100(Fe) and CoS, as well as the variables “*x*” and “*y*” are the mass proportions of MIL-100(Fe) and CoS in the composites, respectively.

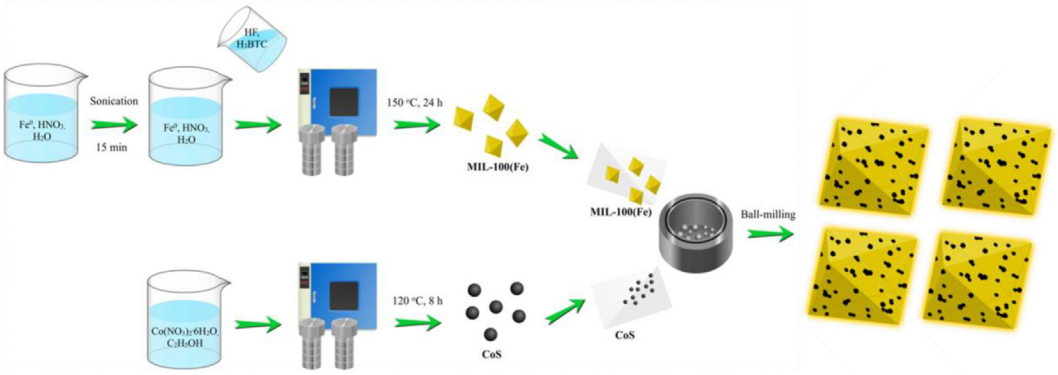

Scheme 1. Schematic fabrication diagram of the MIL-100(Fe)/CoS composites.

2.3. Heterogeneous fenton-like reaction test

The heterogeneous Fenton-like catalysis experiments were accomplished in a 100.0 mL beaker, in which 50.0 mL BPA (10 mg/L) and 10.0 mg catalyst were mixed. After achieving the adsorption-desorption equilibrium within 1 h, a certain amount of H_2O_2 solution was added. During the reaction, 1.5 mL solution was drawn from the reactor with a syringe filter (0.45 μm) at predetermined time intervals for subsequent determinations. 10 μL isopropanol (IPA) was added to the filtrate to remove the excess radicals. The residual BPA concentration in the treated solution was determined at wavelength of 227 nm on an ultra-high performance liquid chromatography (UHPLC, Thermo Scientific Vanquish Flex) equipped with a UV–Vis detector and a C18 reversed-phase column (2.1 mm × 100 mm, 1.7 μm). The detailed determination information can be found in the Electronic supplementary information (ESI).

3. Results and discussion

3.1. Characterizations of MIL-100(Fe)/CoS

The powder X-ray diffraction (PXRD) patterns of MIL-100(Fe), CoS and series M*x*C*y* composites were shown in Fig. 1a. It should be noted that the PXRD patterns of MIL-100(Fe) were well matched with the simulated one (Chen et al., 2020), in which the typical peaks at 10.2° of MIL-100(Fe) became more obvious with the decreasing mass content of CoS. The four characteristic peaks of CoS at $2\theta = 30.6°, 35.4°, 47.0°$ and 54.5° were corresponded to the facets of (100), (101), (102) and (110), respectively (Li et al., 2015), implying that the as-synthesized CoS matches well with the hexagonal phase CoS reported in the previous literature (JCPDS card no. 65–3418) (Zhuang et al., 2018). The M*x*C*y* (especially for M70C30, M50C50 and M30C70) exhibited both crystal phases of MIL-100(Fe) and CoS, in which no extra peaks of crystalline impurities were appeared, suggesting that the structures of MIL-100(Fe) and CoS were maintained well during the ball-milling process.

The compositions of M*x*C*y* were also confirmed by fourier transform infrared (FTIR) analysis. As depicted in Fig. 1b, the peaks at 3423 cm^{-1} and 1113 cm^{-1} are attributed to the O–H vibration C–O stretching vibration of MIL-100(Fe) (Xu et al., 2017). The absorption bands at 1627, 1576, 1447 and 1381 cm^{-1} are ascribed to the carboxyl groups with the $\Delta\nu$ (ν_{as}(COO)-ν_s(COO)) being 180 and 195 cm^{-1}, suggesting that the carboxyl group might be coordinated to the metal ions (Zhang et al., 2012). Furthermore, the peak at 481 cm^{-1} is ascribe to Fe–O stretching vibration (Song et al., 2014), in which the intensity decreased with the decrease of MIL-100(Fe) proportion in M*x*C*y*. The peak at 1176 cm^{-1} is attributed to the Co=S stretching in CoS (Li et al., 2015). As well, the XPS determination displayed obvious peaks of Co 2p, S 2p, S 2s and Fe 2p in M50C50 (Fig. 1c), further affirming the successful interaction of MIL-100(Fe) and CoS.

The morphologies of as-synthesized samples were observed via SEM and TEM. As illustrated in Fig. 2a and e, the original MIL-100(Fe) displays smooth regular octahedron morphology with particle size of ca. 800–2000 nm. After ball-milling, CoS changed from spherical to irregular granular with smaller size (Fig. 2b and f). It could be clearly seen from SEM image (Fig. 2c) and TEM (Fig. 2g

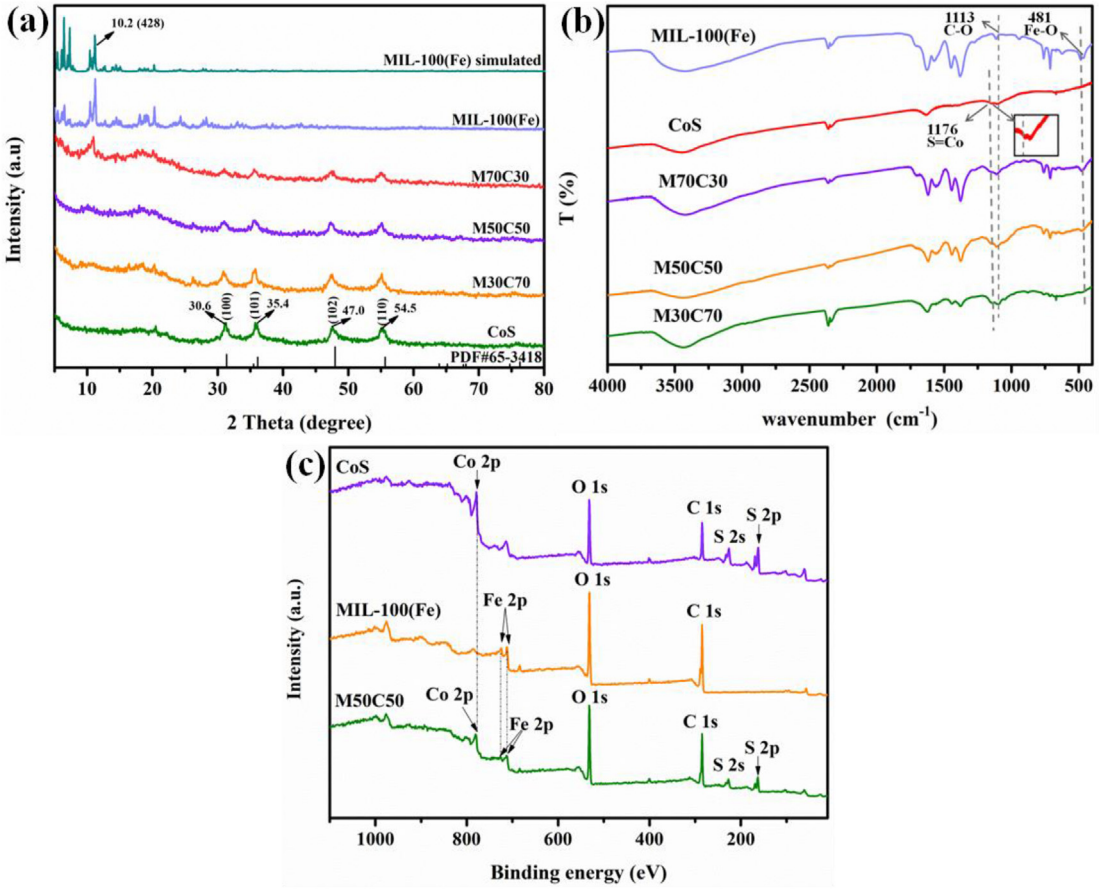

Fig. 1. (a) PXRD patterns, (b) FTIR spectra and (c) XPS spectra of CoS, MIL-100(Fe) and M*x*C*y*.

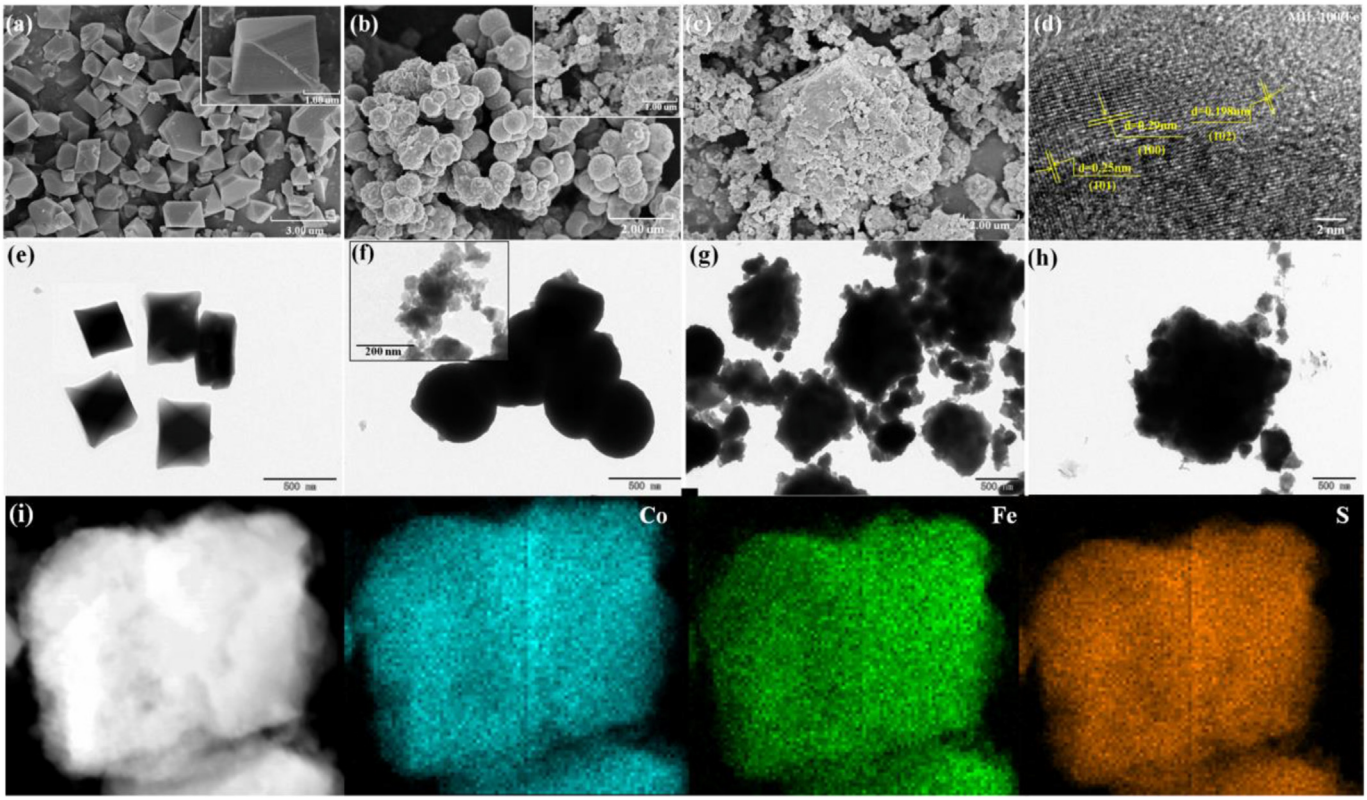

Fig. 2. SEM and TEM images of (a, e) MIL-100(Fe), (b, f) CoS (inset: individual CoS after ball milling treatment) and (c, g, h) M50C50. (d) The HRTEM image of M50C50 composite. (i) TEM element mapping of Co, O and S of the M50C50.

and h) that the surface of MIL-100(Fe) in M50C50 was wrapped by CoS nanoparticles. TEM elemental mapping suggested that Co, Fe and S elements were evenly dispersed in M50C50 (Fig. 2i). The HRTEM image (Fig. 2d) demonstrated the lattice structure of the M50C50 composite, in which the lattice fringes of 0.198 nm, 0.25 nm and 0.29 nm were corresponded to the (102), (101) and (100) lattice plane of CoS (Li et al., 2015; Zhuang et al., 2018), respectively.

3.2. Heterogeneous fenton-like catalytic degradation toward bisphenol A (BPA)

To evaluate the heterogeneous Fenton-like BPA degradation performance of M50C50, series control experiments were carried out. As displayed in Fig. 3a and b, the individual H_2O_2 could hardly remove BPA, which can achieve BPA degradation efficiency of 6.7% within 9 min. Also, only 3.0%, 5.4% and 5.0% BPA were degraded in the presence of MIL-100(Fe)/H_2O_2, CoS/H_2O_2 and individual M50C50 catalyst, respectively. However, quick BPA degradation in all the M*x*C*y*/H_2O_2 systems were observed (Fig. 3a), in which 85.7%, 98.8% and 99.2% BPA degradation efficiencies could be accomplished in the M70C30/H_2O_2, M30C70/H_2O_2 and M50C50/H_2O_2 within 9.0 min, respectively. Moreover, BPA was completely degraded within 12 min with M50C50/H_2O_2. The reaction kinetics of the BPA degradation over different M*x*C*y* catalysts were investigated by pseudo-first-order kinetic ($-\ln[C/C_0] = kt$) (Wu et al., 2020a), in which C, C_0 and k are the surplus BPA concentrations, the original BPA concentration at diverse reaction time and reaction rate constant, respectively. The results revealed that M50C50 can accomplish fastest BPA degradation rate (Fig. 3b) along with the best degradation efficiency.

The significant improvement on BPA degradation over M*x*C*y* composites (especially M50C50) might be contributed to the interfacial microstructure and the synergetic effect between MIL-100(Fe) and CoS. To verify this hypothesis, the BPA degradation activity of the mixture of MIL-100(Fe) and CoS with the identical content ratio as M50C50 in the presence of H_2O_2 (M50C50*/H_2O_2 system in Fig. 3a) was investigated. The results demonstrated that the BPA degradation efficiency in M50C50*/H_2O_2 system was only 9.6% with a low k value of 0.011 min^{-1} in 9 min. A synergistic factor (Λ_{syn}, %) was introduced to explore the synergy effect between MIL-100(Fe) and CoS for BPA degradation (Eq. (1)), which was modified by Chen et al. according to the previous method calculated from rate constant (Chen et al., 2021).

$$\Lambda_{syn} = \frac{R_{M50C50} - (\alpha \times R_{MIL-100(Fe)} + \beta \times R_{CoS})}{R_{M50C50}} \times 100\% \quad (1)$$

where, R_{M50C50}, $R_{MIL\text{-}100(Fe)}$ and R_{CoS} are the final BPA removal efficiency by M50C50, MIL-100(Fe) and CoS, respectively; and α and β are the weight coefficients for MIL-100(Fe) and CoS, respectively. If the $\Lambda_{syn} > 0$, it demonstrated that the synergistic effect happens between the two individual materials. In our case, the calculated Λ_{syn} of M50C50 toward BPA degradation was 95.7% (>0). The high Λ_{syn} value implied that an obvious synergistic effect was occurred between MIL-100(Fe) and CoS in the M50C50 (Nie et al., 2017).

3.3. Influences of reaction conditions

The influences of pH values, M50C50 dosages, H_2O_2 dosages and BPA concentrations toward BPA removal efficiencies were explored, as shown in Fig. 3c to f. The pH is considered to be the extremely

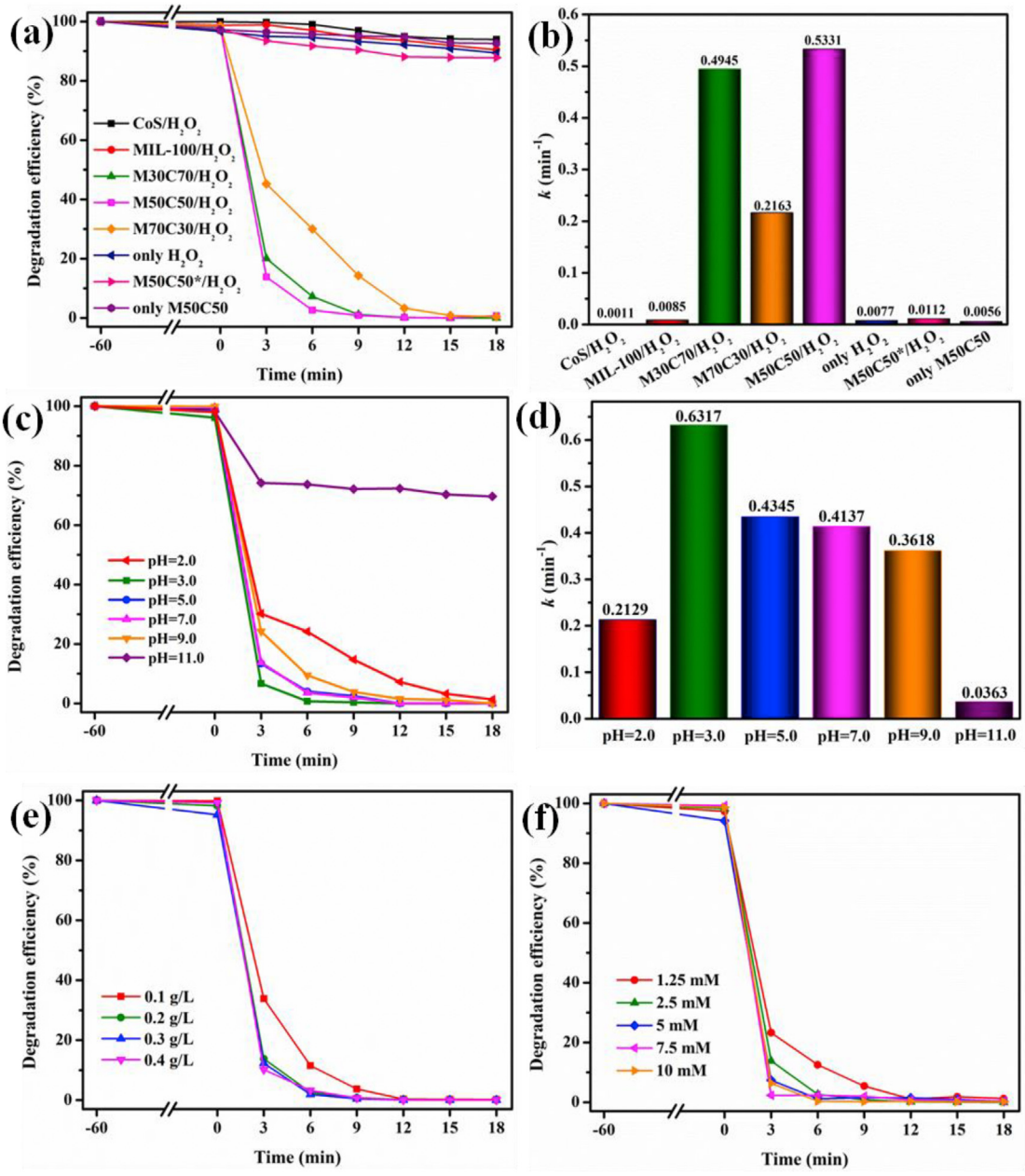

Fig. 3. (a) BPA degradation efficiencies and (b) degradation rates (k values) in different systems. (c) BPA degradation efficiencies and (d) degradation rates (*k* values) of M50C50/H_2O_2 system. The influences of (e) M50C50 dosage and (f) H_2O_2 dosage toward BPA degradation efficiencies. Reaction conditions: MxCy dosage = 0.2 g/L, BPA concentration = 10 mg/L, pH = 5.8 (except Fig. 3c and d), H_2O_2 dosage = 2.5 mM (note: M50C50* in Fig. 3a represents the mixture of MIL-100 (Fe) and CoS with identical content ratio to M50C50).

sensitive factor in a Fenton and Fenton-like reaction (Cao et al., 2018). As seen in Fig. 3c, it can be observed that the pH values exerted negligible influence to BPA adsorption activities of M50C50 in dark conditions (Fig. 3c). The species distribution diagram of BPA molecule (p*K*a = 10.2) (Bautista-Toledo et al., 2005) revealed that the dominating forms of BPA were H_2BPA and deprotonated BPA^{2-} as pH < p*K*a (10.2) and pH > p*K*a, respectively. M50C50 displayed negative surface charge in the pH ranges of 3.0–11.0 (Fig. S1), which couldn't form the strong electrostatic interactions with different BPA species like H_2BPA, $HBPA^-$ and BPA^{2-}. It was observed that M50C50 displayed outstanding BPA removal efficiencies from 96.1% to 99.7% within 9 min in wide pH ranges from 3.0 to 9.0, which were in the pH scope of general wastewater containing organic pollutants (Vojoudi et al., 2018). It was suggested that a too-low or too-high pH is not conducive to Fenton and Fenton-like reaction. Especially, a sharp decrease of BPA degradation efficiency was observed (27.7% within 9 min) when pH was increased to 11.0, which could be due to the H_2O_2 decomposition at alkaline condition (Yi et al., 2019; Wang et al., 2021). As well, M50C50 demonstrated decreasing BPA degradation performance (85.3% within 9 min) with slower degradation rate ($k = 0.213\ min^{-1}$) at pH = 2.0, as the formed $H_3O_2^+$ could control the •OH yield under strong acid conditions like pH < 3.0 (Chen et al., 2009). The biggest BPA degradation rate (*k* value) of M50C50 (Fig. 3d) occurred at pH = 3.0. However, M50C50 displayed identical BPA degradation efficiencies within 9.0 min and similar degradation rates at pH range of

5.0–9.0. From this point, the original pH (pH = 5.8) was chosen in this study for the corresponding BPA degradation experiments considering the degradation efficiency, degradation rate and operating cost.

The influence of M50C50 dosages from 0.1 g/L to 0.4 g/L on the BPA degradation efficiency was investigated. As shown in Fig. 3e, the BPA degradation efficiencies and rates increased gradually to plateau as the M50C50 dosage increased to 0.2 g/L. Furthermore, the corresponding k values were 0.1 g/L (0.361 min^{-1}), 0.2 g/L (0.660 min^{-1}), 0.3 g/L (0.698 min^{-1}) and 0.4 g/L (0.762 min^{-1}), respectively (Fig. S2). It was implied that excessive catalyst could not improve the degradation efficiency effectively. Therefore, the M50C50 dosage of 0.2 g/L was adopted as optimal catalyst dosage to carry out further experiments.

The influence of the H_2O_2 concentration on the BPA degradation was also explored in our study. As shown in Fig. 3f, when the H_2O_2 dosage increased from 1.25 mM to 7.5 mM, the degradation efficiencies increased from 76.8% to 97.7% within 3 min, which can be assigned to the increase of •OH concentration. However, excessive H_2O_2 did not significantly improve the BPA degradation. As the dosages were increased from 7.5 mM to 10.0 mM, the removal efficiencies declined weakly from 97.7% to 93.7%. Also, the k values decreased from 1.259 min^{-1} to 0.921 min^{-1} (Fig. S3). It can be inferred that •OH radicals were consumed by surplus H_2O_2 to form less reactive species (Eq. (2)) and further to inhibit the BPA decomposition (Xu and Wang, 2011).

$$H_2O_2 + {\bullet}OH \rightarrow HOO{\bullet} + H_2O_2 \rightarrow H_2O + O_2 \quad (2)$$

As shown in Fig. S4, M50C50 could accomplish 100% BPA degradation up to the initial concentration of 50.0 mg/L within 18.0 min, implying that M50C50 could be utilized to treat the simulated wastewater containing organics with high concentration.

3.4. Influences of inorganic anions on BPA degradation

Inorganic anions might influence the Fenton or Fenton-like catalysis activity via various mechanism (Chen et al., 2021). It was essential to investigate the influence of different co-existing inorganic ions toward BPA degradation M50C50/H_2O_2 system, considering the practical application in the field of the treatment of real wastewater. Some common anionic inorganic ions like $H_2PO_4^-$, NO_3^- and Cl^- were selected, and the concentrations of inorganic anions were referred from the average water chemical parameters of the surface water in Beijing area (Table. S1) (Yang et al., 2016; Peters et al., 2019). As illustrated in Fig. S5a and S5b, the degradation of BPA was slightly inhibited by the three selected anions. The BPA degradation efficiencies decreased from 99.2% in the wastewater simulated from ultrapure water (without any inorganic ions) to 98.4%, 93.4% and 96.0% in the wastewater samples the presence of $H_2PO_4^-$, NO_3^- and Cl^-, respectively. Accordingly, the k values of the BPA degradation followed the order of no anions (0.533 min^{-1}) > $H_2PO_4^-$ (0.459 min^{-1}) > Cl^- (0.358 min^{-1}) > NO_3^- (0.302 min^{-1}). The inhibited BPA degradation performance with the presence of $H_2PO_4^-$, NO_3^- and Cl^- could be ascribed to that they could react with •OH radicals to generate less active radicals like H_2PO_4•, NO_3• and Cl• following Eqs. (3-5) (Dugandžić et al., 2017; Wang et al., 2018; Yuan et al., 2019).

$$H_2PO_4^- + {\bullet}OH \rightarrow H_2PO_4{\bullet} + OH^- \quad (3)$$

$$NO_3^- + {\bullet}OH \rightarrow NO_3{\bullet} + OH^- \quad (4)$$

$$Cl^- + {\bullet}OH \rightarrow Cl{\bullet} + OH^- \quad (5)$$

3.5. Identification of active species

It was necessary to identify the active species for further understanding the Fenton-like BPA degradation mechanism of M50C50/H_2O_2 system. It was well known that the traditional Fenton and Fenton-like reactions can produce radicals like •OH and $\bullet O_2^-$, as well as singlet oxygen ($^1O_2$) (Deng et al., 2008; Zhao et al., 2017). *Tert*-Butyl alcohol (TBA), 1,4-Benzoquinone (BQ) and L-histidine were usually used as scavengers of •OH, $\bullet O_2^-$ and $^1O_2$, respectively. The BPA degradation efficiency decreased to 63.5% with the addition of TBA (Fig. 4a and b), demonstrating that the •OH radicals were major active species during the Fenton-like reaction. The addition of BQ and L-histidine led to BPA decomposition efficiency decreases by 12.4% and 36.9%, respectively, implying that both $\bullet O_2^-$ and $^1O_2$ acted as synergistic active species to participate the BPA degradation in the M50C50/H_2O_2 system. According to previous reports, $^1O_2$ could be produced from the reactions between $\bullet O_2^-$ and H_2O and •OH (Eqs. (6) and (7)), respectively (Zhu et al., 2019).

$$2{\bullet}O_2^- + 2H_2O \rightarrow H_2O_2 + 2OH^- + {}^1O_2 \quad (6)$$

$$\bullet O_2^- + {\bullet}OH \rightarrow {}^1O_2 + OH^- \quad (7)$$

The active species like •OH, $\bullet O_2^-$ and $^1O_2$ in the H_2O_2 activation process over M50C50 catalyst were further determined by ESR. Dimethyl pyridine N-oxide (DMPO) was adopted to capture •OH in aqueous solution and $\bullet O_2^-$ in methanol solution, respectively. Also, tetramethylpyridine (TEMP) was used to trap $^1O_2$ in the aqueous solution. As illustrated in Fig. 4c-e, the signals of •OH/DMPO, $\bullet O_2^-$/DMPO and $^1O_2$/TEMP adducts were observed, and the signal intensities increased with the time, implying that more active species were yielded in the M50C50/H_2O_2 system as time went on. As well, the signals of •OH/DMPO adducts were also determined in different systems like M50C50/H_2O_2, MIL-100/H_2O_2 and CoS/H_2O_2, in which the intensity in M50C50/H_2O_2 was stronger than those in both MIL-100/H_2O_2 and CoS/H_2O_2 systems, indicating that the synergistic effect occurred between MIL-100(Fe) and CoS. The signals of •OH/DMPO adducts observed in CoS/H_2O_2 system could be attributed to that S^{2-} can activate H_2O_2 to produce •OH (Eq. (8)) (Sun et al., 2004).

$$S^{2-} + 5H_2O_2 \rightarrow 2{\bullet}OH + 4H_2O + SO_4^{2-} \quad (8)$$

Fluorescence method can determine the •OH concentration formed in the AOPs system (Jing et al., 2014), in which terephthalic acid was selected as probe to selectively detect •OH radicals via forming fluorescent 2-hydroxy terephthalic acid. The fluorescent intensity of 2-hydroxy terephthalic acid peak at 426 nm increased with the increase of formed •OH radicals concentration. From Fig. 4f, it could be observed that the peak intensities were weak in the systems like individual H_2O_2, MIL-100/H_2O_2 and CoS/H_2O_2, implying that few •OH radicals were yielded in above-mentioned reaction systems. There is no signal just with the addition of individual M50C50. However, the peak intensities were greatly increased in the presence of both H_2O_2 and MxCy, suggesting that

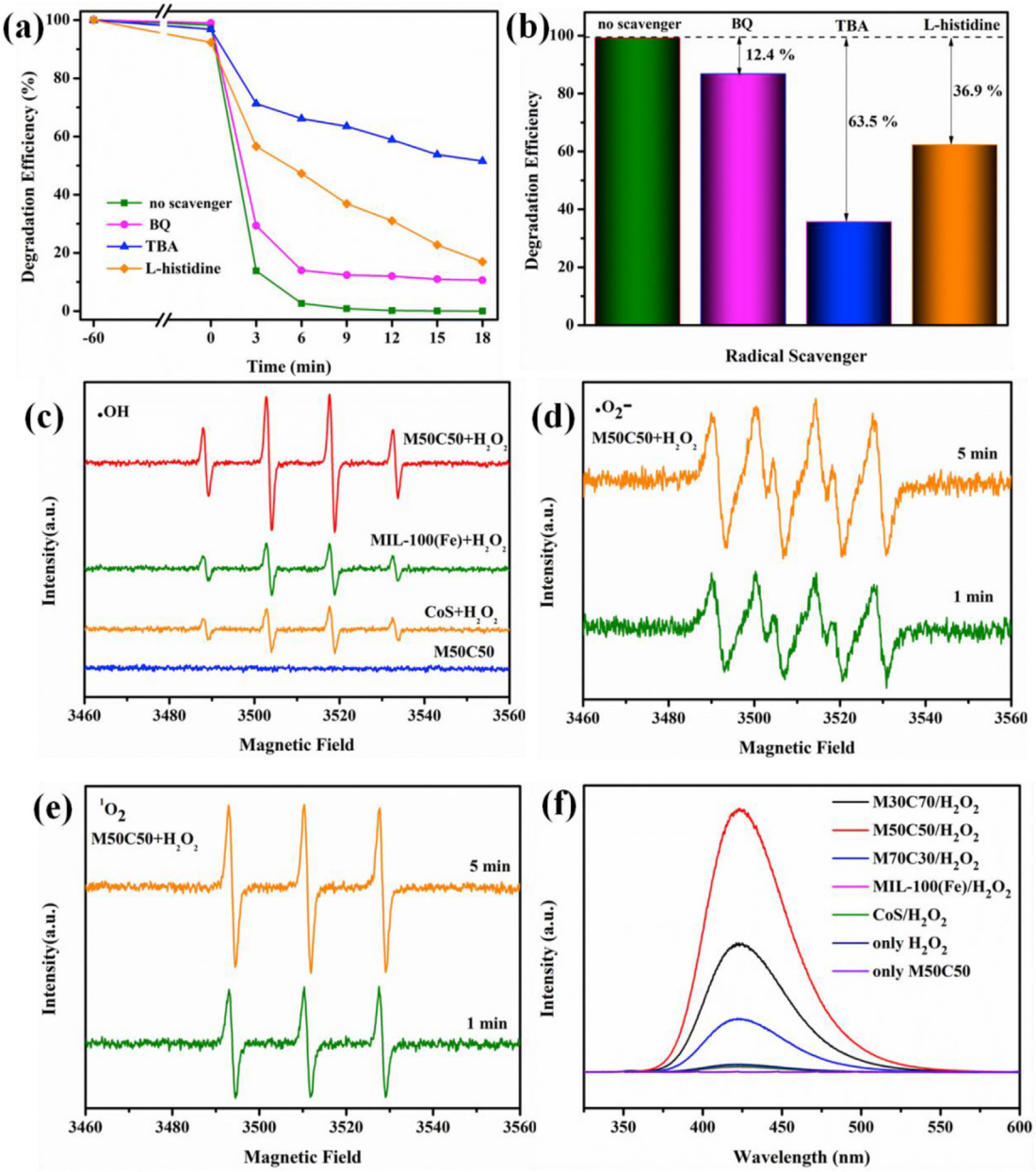

Fig. 4. (a) and (b) Effect of different scavengers on the degradation of BPA over M50C50/H_2O_2 system, ESR spectra of (c) DMPO- •OH, (d) $•O_2^-$ and (e) $^1O_2$ radicals for M50C50. (f) Fluorescence emission spectra of •OH radicals produced during the Fenton-like process at 315 nm over different systems. Condition: M50C50 dosage = 0.2 g/L, BPA concentration = 10 mg/L, pH = 5.8, H_2O_2 dosage = 2.5 mM, TBA concentration = 5 mM, L-histidine or BQ concentration = 2 mM.

H_2O_2 can be effectively activated to produce a large amount of •OH radicals. Additionally, the fluorescence intensities in different M*x*C*y*/H_2O_2 systems were in the order of M50C50/H_2O_2 > M30C70/H_2O_2 > M70C30/H_2O_2, which matched well with the findings of Fig. 3a and b. In previous study (Tai et al., 2004), reaction between •OH radicals and dimethyl sulfoxide (DMSO) can quantitatively produce formaldehyde. Therefore, the quantitative analysis of •OH radicals can be achieved through the determination of the concentration of formaldehyde. It was found that 0.14 mM of •OH radicals were produced in the M50C50/H_2O_2 system within 18.0 min, which were 51 times and 116 times higher than those of CoS/H_2O_2 and MIL-100(Fe)/H_2O_2 systems (Fig. S6), respectively.

3.6. Possible mechanism for H_2O_2 activation over M50C50

Compared with individual CoS and MIL-100(Fe), the Fenton-like reactivities of the series M*x*C*y* were greatly enhanced (Fig. 3a). To investigate the reasons of the improved BPA degradation efficiency over M50C50 with the presence of H_2O_2, XPS were used to explore the surface element information of CoS and M50C50. In the S 2p XPS spectrum of CoS (Fig. 5a), the two broad peaks at 162.40 eV and 168.70 eV can divided into five smaller peaks. The peaks at 161.56 eV and 162.71 eV can be allocated to S^{2-} (Wu et al., 2020b; Ali et al., 2021); the peaks located at 164.46, 168.74 and 170.00 eV could be contributed to S_n^{2-}, SO_4^{2-} and SO_3^{2-}, respectively (Guo et al., 2010; Wu et al., 2020b). The small peak at 165.97 eV in M50C50

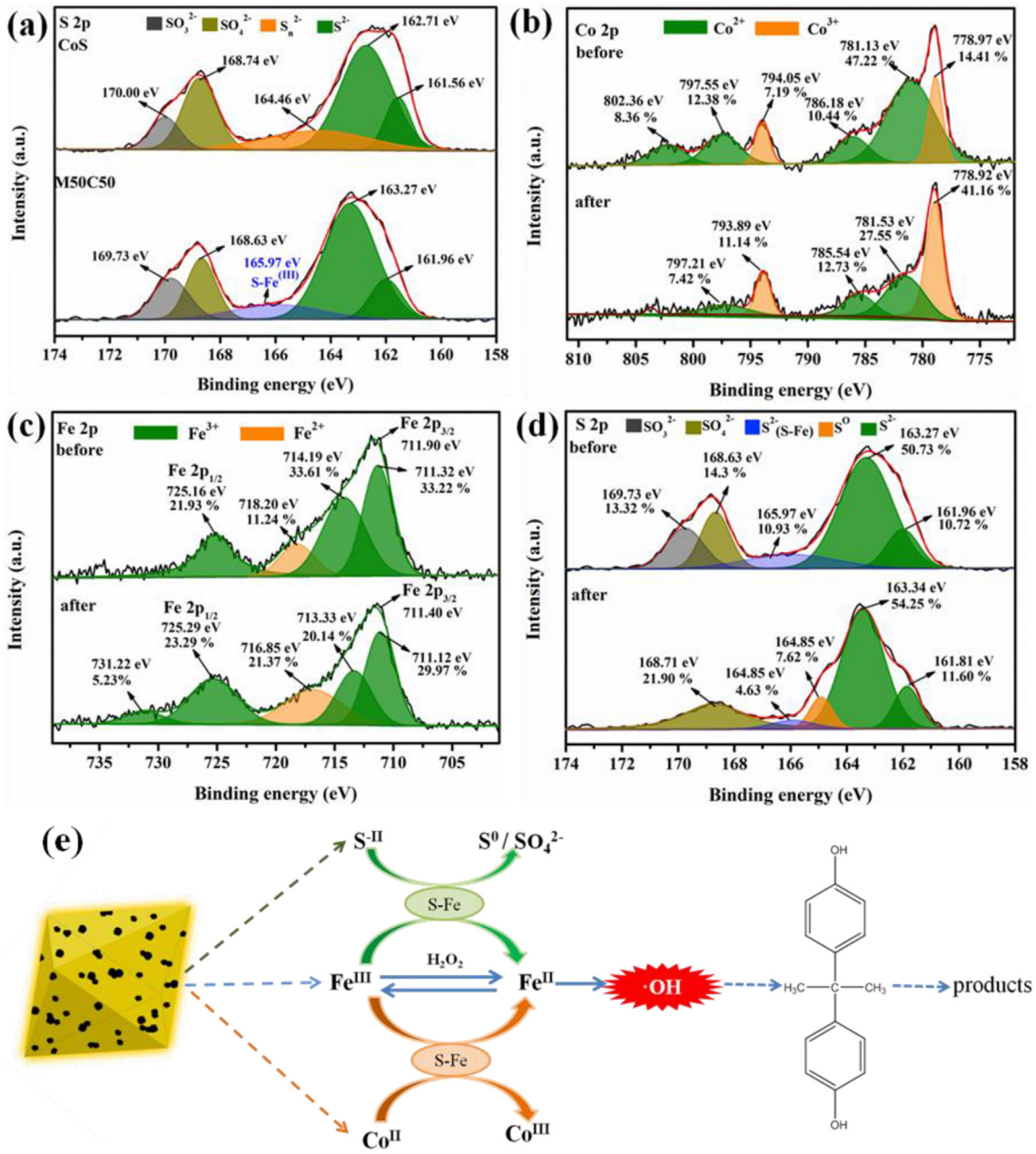

Fig. 5. The fine XPS spectra of (a) S 2p in CoS and M50C50, as well as (b) Co 2p, (c) Fe 2p and (d) S 2p in M50C50 before and after Fenton-like BPA degradation experiments. (e)The possible mechanism for BPA decomposition in the Fenton-like oxidation over M50C50 as catalyst.

could also be observed, which was probably ascribed to the formation of Fe–S bond (Guo et al., 2010). It is considered that the interfacial microstructure and interaction were the key factors for the enhanced performances of composites (Zhong et al., 2020). Therefore, in our case, it can be concluded that Fe–S formed at the interface between MIL-100(Fe) and CoS might lead to the enhanced Fenton-like reactivity of the optimal M50C50. There were not enough S or Fe to form the Fe–S bonding interactions when the proportion of either CoS or MIL-100(Fe) in the M*x*C*y* composites like M70C30 and M30C70 was very low, leading to their poor H_2O_2 activation activity with the evidences of both inferior BPA decomposition efficiency and rate to that of M50C50.

Generally, the •OH formation and the subsequent BPA degradation mainly happen over the catalyst surface in the Fenton-like AOPs (Zhang et al., 2014a). To clarify the corresponding mechanism, XPS analyses were used to determine the chemical states and surface composition of M50C50 before and after the AOPs reaction. The XPS spectra of Co 2p for the fresh and used M50C50 were shown in Fig. 5b. The obvious changes of the two peaks at 778.97 eV and 781.13 eV corresponding to Co^{2+} and Co^{3+} could be observed (Li et al., 2019). Before reaction, Co^{2+} and Co^{3+} contents in fresh M50C50 were 78.4% and 21.6%, which were changed to 47.7% and 52.3% in the used M50C50, respectively. These phenomena suggested that Co^{2+} ions acted as an electron donors in the Fenton-like reaction (Li et al., 2018). As well, the Fe–S bonds at the interface between CoS and MIL-100(Fe) could provide a channel for the electron mobility from Co^{2+} to Fe^{3+} (Eq. (9)), which could accelerate the Fe^{3+}/Fe^{2+} cycle and further boost the BPA degradation efficiency (Hu et al., 2020).

As shown in Fig. 5c, Fe^{3+} is characterized by the Fe 2p peaks at

BE of 711.32 and 725.16 eV (Liu et al., 2009). As well, the two satellite peaks at 714.19 and 731.22 eV suggested that Fe^{2+} ions might also exist in the M50C50 (Noorjahan et al., 2005). While, Fe^{2+} is easily identified by the signal at 718.20 eV (Cappus et al., 1995; Lu et al., 2007). Before and after the Fenton-like reaction, the peak acreages of Fe 2p spectra displayed the relative proportions of iron species. Before Fenton-like reaction, Fe^{2+} and Fe^{3+} contents were ca. 11.2% and 88.8%, respectively. However, after the reaction, Fe^{2+} proportion increased to 21.4%, while Fe^{3+} proportion decreased to 78.6%. These results confirmed the efficient conversion of iron species. Moreover, the transformation from Fe^{3+} to Fe^{2+} was visible via the appearance of the new S^0 peak at 164.85 eV (Fig. 5d), in which the S^{2-} was converted to S^0 via Eq. (11) (Ali et al., 2021). It can be found that S^{2-} content proportion with peak at 164.85 eV decreased from 10.9% in fresh M50C50 to 4.6% in used M50C50, which displayed the sulphur oxidation during the Fenton-like reaction. Similarly, the SO_4^{2-} proportion raised from 14.3% in fresh M50C50 to 21.9% in used M50C50, which was originated from the transformation between Fe^{3+} to Fe^{2+} following Eq. (10) (Zhao et al., 2017).

Based on the above-mentioned XPS analyses, the possible reaction mechanism of H_2O_2 activation over M50C50 was proposed (Fig. 5e). The Fe–S bond improves the Fe^{3+}/Fe^{2+} cycle by two ways: (i) the enhanced transportation of electron from Co to Fe via Fe–S bond coupled with reduction of Fe^{3+} to Fe^{2+} (Eq. (9)) (Hu et al., 2020), which accelerated the Fenton-like reaction rate via the originally rate-limiting step (Eq. (12)); (ii) The redox potential Fe^{3+}/Fe^{2+} (0.70 V/NHE) is greater than that of S^0/S^{2-} (−0.48 V/NHE). Therefore, the sulphur species might draw more electrons from iron, which subsequently produce more Fe^{2+} to activate H_2O_2 for producing •OH (Eqs. 10–12) (Zhao et al., 2017). The effective regeneration of the surface Fe^{2+} by above-mentioned two ways might be responsible for the boosted H_2O_2 activation toward BPA degradation (Eqs. (12) and (13)). To further verify the role of CoS, ZnS was adopted to fabricate MIL-100(Fe)/ZnS composites via ball-milling strategy with the ratio of 1:1. The obtained MIL-100(Fe)/ZnS could only degrade 25.0% BPA within 18 min under the identical conditions (Fig. S7), which was inferior to MIL-100(Fe)/CoS with 100% degradation efficiency. This additional experiment affirmed that the enhanced transportation of electrons from Co to Fe via Fe–S bond led to boosted H_2O_2 activation for BPA degradation.

$$Fe^{3+} + Co^{2+} \rightarrow Fe^{2+} + Co^{3+} \quad (9)$$

$$8Fe^{3+} + 7S^{2-} + 4H_2O \rightarrow 8Fe^{2+} + SO_4^{2-} + 8H^+ \quad (10)$$

$$Fe^{3+} + 7S^{2-} \rightarrow 8Fe^{2+} + S^0 \quad (11)$$

$$Fe^{2+} + H_2O_2 \rightarrow Fe^{3+} + {\cdot}OH + OH^- \quad (12)$$

$$BPA + {\cdot}OH \rightarrow {\cdot} \rightarrow \text{degradation products} \quad (13)$$

3.7. The reusability and stability of M50C50

The recyclability of the catalysts is important for their practical applications. As distinct in Fig. 6a, the BPA degradation efficiencies via Fenton-like reaction over M50C50 were maintained at > 99.0% within 18 min during 5 runs' operations, suggesting that M50C50 possessed potential of long-term application. The leaching Co and Fe concentrations of M50C50 in aqueous solutions after five runs'

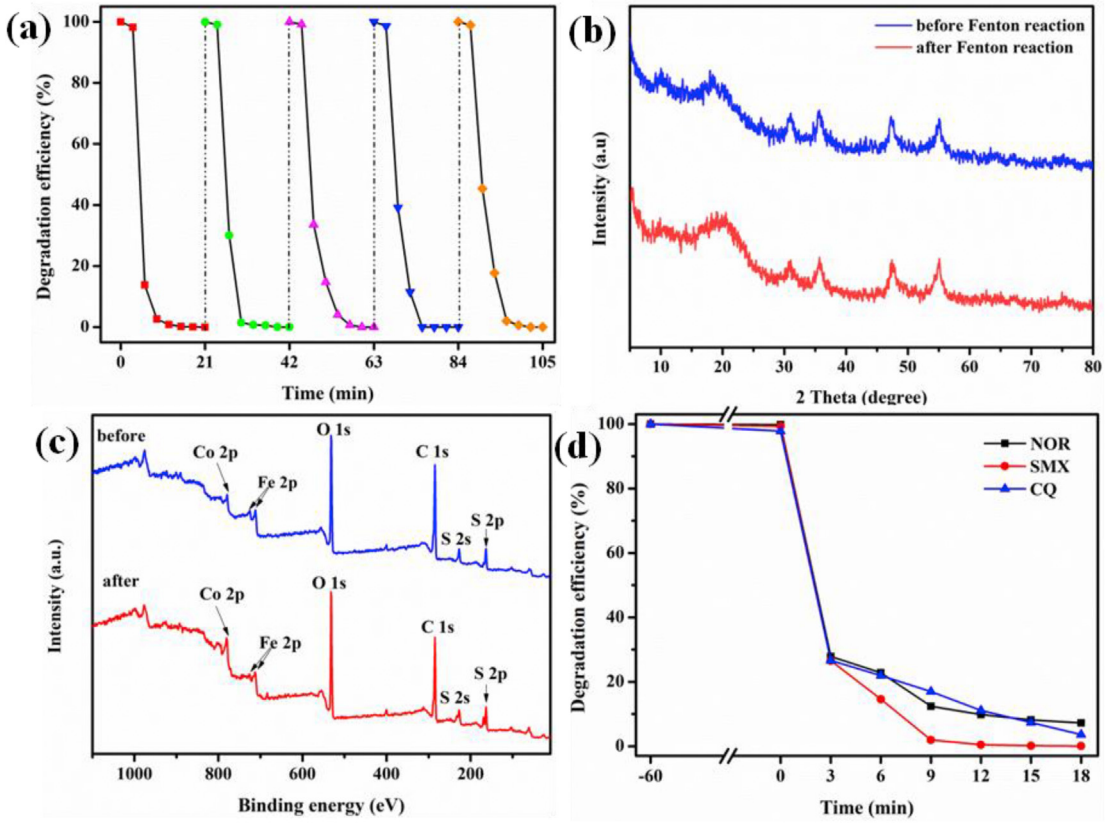

Fig. 6. (a) The cycle experiments of BPA degradation over M50C50, (b) PXRD patterns and (c) XPS survey spectra of M50C50 after degradation experiment, (d) BPA degradation efficiencies (Initial pollutants concentration = 10 mg/L, H_2O_2 dosage = 2.5 mM M50C50 dosage = 0.2 g/L, pH = 5.8).

operations were detected (Table. S2), 1.6% (Fe) and 2.8% (Co) leaching were detected. After Fenton-like reactions, the XRD and XPS images of the used M50C50 matched well with those of the original one (Fig. 6b and c). Besides, the TEM images (Fig. S8) showed no significant changes of the M50C50 morphology, illustrating that the morphology and crystal phase were maintained well.

To highlight the advantages of M50C50 as Fenton-like AOPs catalyst, some counterpart catalysts were selected to compare their BPA degradation activities (Table. S3). Obviously, the M50C50/H_2O_2 system was more efficient for BPA degradation considering the low catalyst dosage (0.2 g/L) and H_2O_2 (2.5 mM) concentration. Furthermore, quick BPA removal was obtained just within 9 min, which is crucial for actual application and energy saving. The degradation efficiencies toward other organic pollutants like norfloxacin (NOR), sulfamethoxazole (SMZ), and chloroquine phosphate (CQ) in M50C50/H_2O_2 system were also assessed. It is found that 92.8% of NOR, 100.0% of SMZ, and 96.4% of CQ could be degraded in 18 min, demonstrating that M50C50 displayed good degradation ability for various organic contaminants. Therefore, M50C50 showed good practical application possibility for sewage water treatment.

4. Conclusions

In summary, series M*x*C*y* composites obtained by facile ball-milling method were adopted as heterogeneous Fenton-like catalysts, which exhibited much higher Fenton catalytic activity towards BPA degradation than MIL-100(Fe) and CoS. The optimum catalyst M50C50 could quickly degrade 100.0% BPA (10 mg/L) within 12 min. The active species capture results and electron spin resonance (ESR) determinations revealed that •OH was the key radicals for BPA decomposition. According to XPS analysis, the regeneration of Fe^{2+} in Fenton-like reaction can be ascribed to that the Fe—S bonds at the interface created the channels for electron transfer. Furthermore, the cycling experiments indicated that M50C50 possessed favourable reusability and stability. This study provides a hopeful strategy to promote the Fe^{2+} regeneration to achieve outstanding organic pollutants degradation efficiency in water treatment.

Author contribution statement

Lin Wu: Data curation, Investigation, Visualization, Writing – original draft. Huifen Fu: Writing – review & editing, Methodology, Validation. Hong-Yu Chu: Software, Drawing. Xiao-Hong Yi: Instrumental, Drawing. Peng Wang: Resources, Instrumental. Chen Zhao: Resources, Software.Chong-Chen Wang: Conceptualization, Funding acquisition, Supervision, Project administration, Writing – review & editing.

Declaration of competing interest

The authors declare that they have no known competing financial interests or personal relationships that could have appeared to influence the work reported in this paper.

Acknowledgements

This work was supported by National Natural Science Foundation of China (51878023, 21806008), Beijing Natural Science Foundation (8202016), Great Wall Scholars Training Program Project of Beijing Municipality Universities (CIT&TCD20180323), BUCEA Post Graduate Innovation Project (PG2020041), Science and Technology General Project of Beijing Municipal Education Commission (KM202110016010) and The Fundamental Research Funds for Beijing University of Civil Engineering and Architecture (X20147/X20141/X20135/X20146).

Appendix A. Supplementary data

Supplementary data to this article can be found online at https://doi.org/10.1016/j.chemosphere.2021.130659.

References

Ali, M., Zhang, X., Idrees, A., Tariq, M., Danish, M., Farooq, U., Shan, A., Jiang, X., Huang, J., Lyu, S., 2021. Advancement in Fenton-like reactions using PVA coated calcium peroxide/FeS system: Pivotal role of sulfide ion in regenerating the Fe(II) ions and improving trichloroethylene degradation. J. Environ. Chem. Eng. 9, 104591.

Bautista-Toledo, I., Ferro-García, M., Rivera-Utrilla, J., Moreno-Castilla, C., Vegas Fernández, F., 2005. Bisphenol A removal from water by activated carbon. Effects of carbon characteristics and solution chemistry. Environ. Sci. Technol. 39, 6246–6250.

Cao, J., Xiong, Z., Lai, B., 2018. Effect of initial pH on the tetracycline (TC) removal by zero-valent iron: adsorption, oxidation and reduction. Chem. Eng. J. 343, 492–499.

Cappus, D., Haßel, M., Neuhaus, E., Heber, M., Rohr, F., Freund, H.-J., 1995. Polar surfaces of oxides: reactivity and reconstruction. Appl. Surf. Sci. 337, 268–277.

Chen, D.-D., Yi, X.-H., Zhao, C., Fu, H., Wang, P., Wang, C.-C., 2020. Polyaniline modified MIL-100(Fe) for enhanced photocatalytic Cr(VI) reduction and tetracycline degradation under white light. Chemosphere 245, 125659.

Chen, L., Ji, H., Qi, J., Huang, T., Wang, C.-C., Liu, W., 2021. Degradation of acetaminophen by activated peroxymonosulfate using $Co(OH)_2$ hollow microsphere supported titanate nanotubes: insights into sulfate radical production pathway through $CoOH^+$ activation. Chem. Eng. J. 406, 126877.

Chen, Q., Wu, P., Li, Y., Zhu, N., Dang, Z., 2009. Heterogeneous photo-Fenton photodegradation of reactive brilliant orange X-GN over iron-pillared montmorillonite under visible irradiation. J. Hazard Mater. 168, 901–908.

Deng, J., Jiang, J., Zhang, Y., Lin, X., Du, C., Xiong, Y., 2008. $FeVO_4$ as a highly active heterogeneous Fenton-like catalyst towards the degradation of Orange II. Appl. Catal. B Environ. 84, 468–473.

Dugandžić, A.M., Tomašević, A.V., Radišić, M.M., Šekuljica, N.Ž., Mijin, D.Ž., Petrović, S.D., 2017. Effect of inorganic ions, photosensitisers and scavengers on the photocatalytic degradation of nicosulfuron. J. Photochem. Photobiol. Chem. 336, 146–155.

Gao, C., Chen, S., Quan, X., Yu, H., Zhang, Y., 2017. Enhanced Fenton-like catalysis by iron-based metal organic frameworks for degradation of organic pollutants. J. Catal. 356, 125–132.

Guo, K., Wu, Z., Shang, C., Yao, B., Hou, S., Yang, X., Song, W., Fang, J., 2017. Radical chemistry and structural relationships of PPCP degradation by UV/chlorine treatment in simulated drinking water. Environ. Sci. Technol. 51, 10431–10439.

Guo, L., Chen, F., Fan, X., Cai, W., Zhang, J., 2010. S-doped α-Fe_2O_3 as a highly active heterogeneous Fenton-like catalyst towards the degradation of acid orange 7 and phenol. Appl. Catal. B Environ. 96, 162–168.

Hao, J., Zhang, Q., Chen, P., Zheng, X., Wu, Y., Ma, D., Wei, D., Liu, H., Liu, G., Lv, W., 2019. Removal of pharmaceuticals and personal care products (PPCPs) from water and wastewater using novel sulfonic acid (-SO_3H) functionalized covalent organic frameworks. Environ. Sci. Nano. 6, 3374–3387.

Hu, S., Li, Y., Zang, C., Ma, X., Zhao, B., Chen, F., 2020. Piezoelectric field-promoted heterogeneous sono-Fenton performance of MoS_2/α-Fe_2O_3 heterojunction structure. Appl. Surf. Sci. 534, 147499.

Ike, I.A., Karanfil, T., Cho, J., Hur, J., 2019. Oxidation byproducts from the degradation of dissolved organic matter by advanced oxidation processes-A critical review. Water Res. 164, 114929.

Jing, H.-P., Wang, C.-C., Zhang, Y.-W., Wang, P., Li, R., 2014. Photocatalytic degradation of methylene blue in ZIF-8. RSC Adv. 4, 54454–54462.

Li, J., Li, X., Han, J., Meng, F., Jiang, J., Li, J., Xu, C., Li, Y., 2019. Mesoporous bimetallic Fe/Co as highly active heterogeneous Fenton catalyst for the degradation of tetracycline hydrochlorides. Sci. Rep. 9, 15820.

Li, J., Miao, J., Duan, X., Dai, J., Liu, Q., Wang, S., Zhou, W., Shao, Z., 2018. Fine-tuning surface properties of perovskites via nanocompositing with inert oxide toward developing superior catalysts for advanced oxidation. Adv. Funct. Mater. 28, 1804654.

Li, R., Wang, S., Wang, J., Huang, Z., 2015. Ni_3S_2@CoS core–shell nano-triangular pyramid arrays on Ni foam for high-performance supercapacitors. Phys. Chem. Chem. Phys. 17, 16434–16442.

Liu, T., You, H., Chen, Q., 2009. Heterogeneous photo-Fenton degradation of polyacrylamide in aqueous solution over Fe(III)-SiO_2 catalyst. J. Hazard Mater. 162, 860–865.

Lu, L., Ai, Z., Li, J., Zheng, Z., Li, Q., Zhang, L., 2007. Synthesis and characterization of Fe-Fe_2O_3 core-shell nanowires and nanonecklaces. Cryst. Growth Des. 7, 459–464.

Mosteo, R., Ormad, M., Ovelleiro, J., 2007. Photo-Fenton processes assisted by solar light used as preliminary step to biological treatment applied to winery

wastewaters. Water Sci. Technol. 56, 89–94.
Nidheesh, P.V., Gandhimathi, R., Ramesh, S.T., 2013. Degradation of dyes from aqueous solution by Fenton processes: a review. Environ. Sci. Pollut. Res. 20, 2099–2132.
Nie, G., Huang, J., Hu, Y., Ding, Y., Han, X., Tang, H., 2017. Heterogeneous catalytic activation of peroxymonosulfate for efficient degradation of organic pollutants by magnetic Cu^0/Fe_3O_4 submicron composites. Chin. J. Catal. 38, 227–239.
Noorjahan, M., Kumari, V.D., Subrahmanyam, M., Panda, L., 2005. Immobilized Fe(III)-HY: an efficient and stable photo-Fenton catalyst. Appl. Catal. B Environ. 57, 291–298.
Peng, L., Duan, X., Shang, Y., Gao, B., Xu, X., 2021. Engineered carbon supported single iron atom sites and iron clusters from Fe-rich Enteromorpha for Fenton-like reactions via nonradical pathways. Appl. Catal. B Environ. 287, 119963.
Peters, M., Guo, Q., Strauss, H., Wei, R., Li, S., Yue, F., 2019. Contamination patterns in river water from rural Beijing: a hydrochemical and multiple stable isotope study. Sci. Total Environ. 654, 226–236.
Pouran, S.R., Raman, A.A.A., Daud, W.M.A.W., 2014. Review on the application of modified iron oxides as heterogeneous catalysts in Fenton reactions. J. Clean. Prod. 64, 24–35.
Shayegan, Z., Lee, C.-S., Haghighat, F., 2018. TiO_2 photocatalyst for removal of volatile organic compounds in gas phase-A review. Chem. Eng. J. 334, 2408–2439.
Sun, D., Wang, L., Ruan, D., 2004. Indirect determination of trace sulfide in water by extraction-catalytic kinetic spectrophotometry. Chin. J. Anal. Chem. 32, 179–182.
Song, G., Wang, Z., Wang, L., Li, G., Huang, M., Yin, F., 2014. Preparation of MOF(Fe) and its catalytic activity for oxygen reduction reaction in an alkaline electrolyte. Chin. J. Catal. 35, 185–195.
Tai, C., Peng, J.-F., Liu, J.-F., Jiang, G.-B., Zou, H., 2004. Determination of hydroxyl radicals in advanced oxidation processes with dimethyl sulfoxide trapping and liquid chromatography. Anal. Chim. Acta 527, 73–80.
Umar, M., Aziz, H.A., Yusoff, M.S., 2010. Trends in the use of Fenton, electro-Fenton and photo-Fenton for the treatment of landfill leachate. Waste Manag. 30, 2113–2121.
Vasiliadou, I.A., Molina, R., Martínez, F., Melero, J.A., 2013. Biological removal of pharmaceutical and personal care products by a mixed microbial culture: sorption, desorption and biodegradation. Biochem. Eng. J. 81, 108–119.
Vojoudi, H., Badiei, A., Amiri, A., Banaei, A., Ziarani, G., Schenk-Joß, K., 2018. Efficient device for the benign removal of organic pollutants from aqueous solutions using modified mesoporous magnetite nanostructures. J. Phys. Chem. Solid. 113, 210–219.
Wang, C.-C., Wang, X., Liu, W., 2019. The synthesis strategies and photocatalytic performances of TiO_2/MOFs composites: a state-of-the-art review. Chem. Eng. J. 123601.
Wang, C., Xue, Y., Wang, P., Ao, Y., 2018. Effects of water environmental factors on the photocatalytic degradation of sulfamethoxazole by AgI/UiO-66 composite under visible light irradiation. J. Alloys Compd. 748, 314–322.
Wang, J.-W., Qiu, F.-G., Wang, P., Ge, C., Wang, C.-C., 2021. Boosted bisphenol A and Cr(VI) cleanup over Z-scheme WO_3/MIL-100(Fe) composites under visible light. J. Clean. Prod. 279, 123408.
Wang, J., Zhuan, R., 2020. Degradation of antibiotics by advanced oxidation processes: an overview. Sci. Total Environ. 701, 135023.
Watts, R.J., Teel, A.L., 2005. Chemistry of modified Fenton's reagent (catalyzed H_2O_2 propagations-CHP) for in situ soil and groundwater remediation. J. Environ. Eng. 131, 612–622.
Wu, L., Fu, H., Wei, Q., Zhao, Q., Wang, P., Wang, C.-C., 2020a. Porous $Cd_{0.5}Zn_{0.5}S$ nanocages derived from ZIF-8: boosted photocatalytic performances under LED-visible light. Environ. Sci. Pollut. Res. 28, 5218–5230.
Wu, X., Zhao, W., Huang, Y., Zhang, G., 2020. A mechanistic study of amorphous CoS*x* cages as advanced oxidation catalysts for excellent peroxymonosulfate activation towards antibiotics degradation. Chem. Eng. J. 381, 122768.
Xiao-Hong, Y., Chong-Chen, W., 2020. Elimination of emerging organic contaminants in wastewater by advanced oxidation process over iron-based MOFs and their composites. Prog. Chem. 3, 471–489.
Xu, L., Wang, J., 2011. A heterogeneous Fenton-like system with nanoparticulate zero-valent iron for removal of 4-chloro-3-methyl phenol. J. Hazard Mater. 186, 256–264.
Xu, X.-Y., Chu, C., Fu, H., Du, X.-D., Wang, P., Zheng, W., Wang, C.-C., 2018. Light-responsive UiO-66-NH_2/Ag_3PO_4 MOF-nanoparticle composites for the capture and release of sulfamethoxazole. Chem. Eng. J. 350, 436–444.
Xu, X., Liu, R., Cui, Y., Liang, X., Lei, C., Meng, S., Ma, Y., Lei, Z., Yang, Z., 2017. PANI/FeUiO-66 nanohybrids with enhanced visible-light promoted photocatalytic activity for the selectively aerobic oxidation of aromatic alcohols. Appl. Catal. B Environ. 210, 484–494.
Yang, L., He, J., Liu, Y., Wang, J., Jiang, L., Wang, G., 2016. Characteristics of change in water quality along reclaimed water intake area of the Chaobai River in Beijing, China. J. Environ. Sci. 50, 93–102.
Yap, C.L., Gan, S., Ng, H.K., 2011. Fenton based remediation of polycyclic aromatic hydrocarbons-contaminated soils. Chemosphere. 83, 1414–1430.
Yi, Q., Ji, J., Shen, B., Dong, C., Liu, J., Zhang, J., Xing, M., 2019. Singlet oxygen triggered by superoxide radicals in a molybdenum cocatalytic Fenton reaction with enhanced REDOX activity in the environment. Environ. Sci. Technol. 53, 9725–9733.
Yuan, R., Zhu, Y., Zhou, B., Hu, J., 2019. Photocatalytic oxidation of sulfamethoxazole in the presence of TiO_2: effect of matrix in aqueous solution on decomposition mechanisms. Chem. Eng. J. 359, 1527–1536.
Zhang, T.-z., Lu, Y., Li, Y.-g., Zhang, Z., Chen, W.-l., Fu, H., Wang, E.-b., 2012. Metal-organic frameworks constructed from three kinds of new Fe-containing secondary building units. Inorg. Chim. Acta. 384, 219–224.
Zhang, X., Ding, Y., Tang, H., Han, X., Zhu, L., Wang, N., 2014. Degradation of bisphenol A by hydrogen peroxide activated with $CuFeO_2$ microparticles as a heterogeneous Fenton-like catalyst: efficiency, stability and mechanism. Chem. Eng. J. 236, 251–262.
Zhang, Y., Zhang, F., Yang, Z., Xue, H., Dionysiou, D.D., 2016. Development of a new efficient visible-light-driven photocatalyst from SnS_2 and polyvinyl chloride. J. Catal. 344, 692–700.
Zhang, Y.C., Yao, L., Zhang, G., Dionysiou, D.D., Li, J., Du, X., 2014b. One-step hydrothermal synthesis of high-performance visible-light-driven SnS_2/SnO_2 nanoheterojunction photocatalyst for the reduction of aqueous Cr(VI). Appl. Catal. B Environ. 144, 730–738.
Zhao, L., Chen, Y., Liu, Y., Luo, C., Wu, D., 2017. Enhanced degradation of chloramphenicol at alkaline conditions by S(-II) assisted heterogeneous Fenton-like reactions using pyrite. Chemosphere 188, 557–566.
Zhong, Z., Li, M., Fu, J., Wang, Y., Muhammad, Y., Li, S., Wang, J., Zhao, Z., Zhao, Z., 2020. Construction of Cu-bridged Cu_2O/MIL(Fe/Cu) catalyst with enhanced interfacial contact for the synergistic photo-Fenton degradation of thiacloprid. Chem. Eng. J. 395, 125184.
Zhou, P., Ren, W., Nie, G., Li, X., Duan, X., Zhang, Y., Wang, S., 2020. Fast and long-lasting iron (III) reduction by boron toward green and accelerated Fenton chemistry. Angew. Chem. 132, 16660–16669.
Zhu, Y., Zhu, R., Xi, Y., Zhu, J., Zhu, G., He, H., 2019. Strategies for enhancing the heterogeneous Fenton catalytic reactivity: a review. Appl. Catal. B Environ. 255, 117739.
Zhuang, G., Liu, H., Chen, X., 2018. High-performance dye-sensitized solar cells using Ag-doped CoS counter electrodes. RSC Adv. 8, 18792–18799.
Zou, J., Ma, J., Chen, L., Li, X., Guan, Y., Xie, P., Pan, C., 2013. Rapid acceleration of ferrous iron/peroxymonosulfate oxidation of organic pollutants by promoting Fe(III)/Fe(II) cycle with hydroxylamine. Environ. Sci. Technol. 47, 11685–11691.